Supporting information:

Coexistence of the Radial-Guided Mode and WGM in Azimuthal-Grating-Integrated Microring Lasers

Jinghan Chen,[1] Abdul Nasir,[1] Adrian Abazi,[2,3,4] Alexander Eich,[2,3,4] Alejandro Sánchez-Postigo,[2,3,4] Harunobu Takeda,[1] Yuya Mikami,[1] Naoya Tate,[1] Yuji Oki,[1] Yohei Yamamoto,[5] Carsten Schuck,[2,3,4] and Hiroaki Yoshioka[1]*

[1]Graduate School and Faculty of Information Science and Electrical Engineering, Kyushu University, Fukuoka 819-0395, Japan.

[2]Department for Quantum Technology, University of Münster, Münster 48149, Germany.

[3]Center for Soft Nano Science (SoN), Münster 48149, Germany.

[4]Center for NanoTechnology (CeNTech), Münster 48149, Germany.

[5]Department of Materials Science, Institute of Pure and Applied Sciences, and Tsukuba Research Center for Energy Materials Science (TREMS), University of Tsukuba, Tsukuba, Ibaraki 305-8573, Japan.

Theoretical detail in modes generation mechanism

Referring to the wave equation for electromagnetic waves in cylindrical coordinates (r, ϕ, z):

$$\nabla^2 E + \mathrm{k}^2 E = 0. \quad (1)$$

Since the electric field is cylindrically symmetric, we can separate variables in the wave equation:

$$E(r, \phi, z) = R(r)\Phi(\phi)Z(z). \quad (2)$$

This results in independent equations for the radial, angular, and axial components. The radial part of the equation can be expressed as Bessel's differential equation:

$$\frac{1}{r}\frac{d}{d_r}\left(r\frac{dR}{d_r}\right)+(k_r^2-\frac{m^2}{r^2})R=0. \quad (3)$$

Its solution is the Bessel function:

$$R(r)=J_m(k_r)=0, \quad (4)$$

where J_m is the Bessel function of the first kind of order **m**, and k_r is the radial wave vector.

The azimuthal part satisfies the following equation:

$$\frac{\mathrm{d}^2\Phi}{d\phi^2}+m^2\Phi=0. \quad (5)$$

Its solution is $\Phi_{(\phi)}=e^{im\phi}$. Since the thickness of the microring is very small, the axial mode distribution can be neglected. Combining all the parts and including the time dependence, the wave function of the radial mode can be expressed as:

$$\Psi_{\mathrm{Radial}}(r,\phi,t) = AJ_{\boldsymbol{m}}(k_rR)e^{i\boldsymbol{m}\phi}e^{-i\omega t}. \quad (6)$$

Under typical conditions, the dominant radial mode can be estimated using the effective refractive index n_{eff}, boundary conditions R, and the gain wavelength range of the active material. The leading radial mode is determined by identifying the azimuthal order that satisfies $J_{\boldsymbol{m}}(k_rR)$=0. It can also be reduced to the propagation of wave vectors, where the propagation of radial wave vectors still satisfies the generation of conventional standing wave modes. The radial wave vector k_r is given by $k_r=\frac{\xi_{m,n}}{R}$, where $\xi_{\mathrm{m,n}}$ are the solutions of $J_{\boldsymbol{m}}(k_rR)$=0, and $\boldsymbol{m}=0$ or 1 . Additionally, for a given microring, the wave vector is related to the standing wave condition as: $k_r=\frac{2\pi n_{eff}}{\lambda}$. Rearranging, we get: $\xi_{\mathbf{m,n}}\lambda=$

$2\pi n_{\text{eff}}$. For integer **n**, this can be written as $2Rn_{\text{eff}} = \boldsymbol{n}\lambda$, which is also the standing wave condition in a cavity length with 2*R*. The free spectral range (FSR) of the fundamental modes is:

$$\Delta\lambda_{\text{radial}} = \frac{\lambda^2}{4n_{\text{eff}}R}. \quad (7)$$

In microrings with small radii, radial modes are primarily governed by low-order Bessel functions. The zero-order Bessel function exhibits a peak at the center of the circle (*R*=0). Due to the characteristics of the zero-order Bessel function and the first-order Bessel function—the zero-order Bessel function is peaked at the center of the circle, while the first-order Bessel function is zero at the center of the circle and is symmetric about the center—it can be further concluded that for radial modes, the modes can be described by the zero-order Bessel function (J_0) when the optical length is an odd multiple of the light wavelength (odd mode), while the modes can be described by the first-order Bessel function (J_1) when the optical length is an even multiple of the mode wavelength (even mode)[1]. These modal properties are influenced by the boundary conditions and n_{eff} of the microring, which together determine whether the fundamental mode within a given wavelength range is an even or odd mode. In conclusion, for an active cladding microring, the dominant radial mode can be estimated using the n_{eff}, boundary conditions, and the gain wavelength range of the active material.

Moreover, in this active layer, light waves do not undergo total internal reflection at the junction between the circular active layer and the microring, which is necessary for the formation of whispering gallery modes (WGMs). This occurs because light is not reflected when it travels from the low refractive index of the active layer into the high refractive index of the microring; instead, it is scattered

into the microring. As a result, there is no WGM propagating along the edges of the active layer, and no high-order WGMs are formed. However, as the dimensions increase and the modes become more complex, the emergence of radial modes with high azimuthal order is expected.

When the light wave propagates in a high n_{eff} microring, the radially propagating wavevector k_r is gradually transformed into an angularly propagating wavevector k_ϕ after many reflections. This transformation occurs due to the microring's geometry and boundary conditions, which guide the light within the ring. In such microrings, the light wave is confined and propagates minimally in the radial direction due to the narrow ring width, while it resonates along the circumference. Each reflection reduces the radial component k_r as the light path adjusts to maximize its length within the ring [2]. The microring supports specific resonant modes, particularly WGMs, where light circulates the circumference with minimal radial leakage. This resonance favors propagation paths with strong angular components, aligning the wavevector more with the ring's circumference over time. Consequently, the energy of the radial mode is converted into the energy of the angular mode, forming a WGM.

The wave travels in the circumferential direction, undergoing total internal reflection along the outer sidewall, with the field being radially confined. This primarily results in standing waves forming in the angular direction. The angular mode number $\boldsymbol{m}$ represents the number of wavelengths around the circumference and corresponds to the order of the Bessel function. The angular phase transition translates into an angular wave vector $k_\phi = \frac{\boldsymbol{m}}{R}$, representing the propagation constant in the circumferential direction. In the radial direction, only one node

exists, corresponding to the first zero of this type of Bessel function. The radial wave vector $k_r = \frac{\xi_{\mathbf{m},1}}{R}$. The wave function of the WGM can be expressed as:

$$\Psi_{\mathrm{WGM}}(r,\phi,t) = AJ_{\boldsymbol{m}}(k_r R)e^{i(\boldsymbol{m}\phi-\omega t)}$$

$$= AJ_{\boldsymbol{m}}\left(\xi_{\mathbf{m},1}\right)e^{i(k_\phi R\phi-\omega t)}. \quad (8)$$

The angular wave vector $k_\phi = \frac{\boldsymbol{m}}{R}$ also satisfies $k_\phi = \frac{2\pi n_{eff}}{\lambda}$ as a propagating constant. For integer $\boldsymbol{m}$, it satisfies $2\pi R n_{\mathrm{eff}} = \boldsymbol{m}\lambda$, and the FSR of the WGMs is:

$$\Delta\lambda_{\mathrm{WGM}} = \frac{\lambda^2}{2\pi n_{\mathrm{eff}} R}. \quad (9$$

In summary, this simulation highlights the formation of cylinder waves formation in micoring structures with an out-clad active layer. The next part mainly discusses how the grating structure influences the cylinder waves.

According to Huygens' principle, when light is incident on a grating, the secondary spherical waves produced by each grating element interfere with each other, forming an interference pattern. Each grating element has a fixed phase difference in the angular direction, resulting in constructive interference of the secondary waves in specific directions determined by the grating period, thereby producing enhanced light intensity at these positions, known as the diffraction maxima. At this point, the wave vector points towards the distribution of the diffraction maxima. When the bulk wave from the center of the microring, described by a Bessel function, is incident on the microring and the azimuthal grating, cylindrical waves with angular and radial wave vector components are produced, and the resonance mode is related to the grating period.

For radial modes, the boundary condition of the microring is not simply R but can be described by $R(\phi) = R - d_g \cos(\boldsymbol{M}\phi)$, where $0 \leq \phi < 2\pi$, d_g is the grating depth, and **M** is the number of grating elements. The radial mode can then be described by the following formula:

$$\Psi_{\text{Radial}}(r, \phi, t) = AJ_{\boldsymbol{m}}\big(k_r(R - d_g \cos(\boldsymbol{M}\phi))\big)e^{i\boldsymbol{m}\phi}e^{-i\omega t}. \quad (10)$$

By simplifying this complex secondary wave interference to the wave vector condition, and when the microring size is relatively large (i.e., the curvature is much larger than the grating period, with the number of grating elements around the microring exceeding 50 [3,4]), the CMT for DFB structure can be used to simplify the calculation on how the grating parameter influence the guide-mode resonance (GMR) mode.

However, it is necessary to quantitatively evaluate and compensate for the bending loss for diffraction waves propagating on the grating. For the microring and grating, the bending loss coefficient of a curved waveguide can be simplified and evaluated by $\alpha = Ae^{(-B/\boldsymbol{R})}$ [5], where A and B depend on the material properties. Furthermore, when light is incident radially (at an incident angle of 0˚) and the substrate thickness beneath the grating is very small, resulting in negligible phase shift, multiple diffraction orders emerge in various directions, with the first-order and second-order diffractions being the most prominent. According to the Bragg condition, the first-order diffraction exits radially (with a diffraction angle of 0˚), while the second-order diffraction exits angularly (with a diffraction angle of 90˚). Within the microring, light primarily propagates in the angular direction, allowing the second-order diffraction to more easily couple with the propagating light and resonate, forming GMR modes. Considering the bending loss of the grating during

feedback, the wavelength of the GMR is determined by the Bragg condition for the bent second-order diffraction, expressed as:

$$\lambda_{\mathrm{GMR}} = (1 - \alpha) n_{\mathrm{eff}} \Lambda. \quad (11)$$

Simulation on OAM WGMs carried.

When the WGMs in the microring possess an azimuthal mode number $\boldsymbol{m}$, the $\boldsymbol{M}$ numbers of grating elements on the inner wall periodically modulate the phase of the optical field. This modulation effect can be understood as the phase accumulation of the optical field along the circular path. If $\boldsymbol{M} = \boldsymbol{m}+l$, then after modulation by the gratings in the microring, the phase of the optical field will accumulate an additional phase shift of $2\pi l$. This extra phase shift causes the scattered optical field to carry l units of topological charge, thereby generating an OAM-carrying beam with a topological charge of l. This is the reason why grating integrated microrings are used as the usual method for integratable OAM emitters.

However, WGMs exhibit both Transverse Magnetic (TM) and Transverse Electric (TE) modes, which can propagate in both clockwise (CW) and counterclockwise (CCW) directions. From simulation results on microring without grating, the eigen TM modes around 600 nm have an azimuthal mode number $\boldsymbol{m}$=98, and the eigen TE modes around 600 nm have an azimuthal mode number $\boldsymbol{m}$=83. The difference in $\boldsymbol{m}$ between TE and TM modes is due to different n_{eff}, respectively. In this structure, the n_{eff} of TM modes is lower because their electric field is distributed in the microring core and the lower refractive index active coating and substrate. Figures S1(A) and S1(C) show the normalized xy-component and phase image of the electric field for the TE mode with a topological charge l=1 ($\boldsymbol{M}$=84). When subjected to periodic scatterer modulation,

these components interact to form a complex interference pattern. This modulation results in an interference field resembling a radial mode, indicating stronger coupling between the radial mode and WGM due to scattering from the grating. The phase image shown in Fig. S1(C) demonstrates the interference of phase variations in the CW and CCW directions, leading to mutual cancellation and resulting in negligible OAM.

Figures S1(B) and S1(D) display the normalized z-component and phase image of the electric field for the TM mode with a topological charge l=1(M=99). Here, the electric field is oriented axially, and the phase variations directly add up, unaffected by the cancellation effects seen in the TE mode. This results in a helical

phase structure, as shown in the phase image in Fig. S1(D), indicating a layering of phase shift from $-\pi$ to π in the CW and CCW directions.

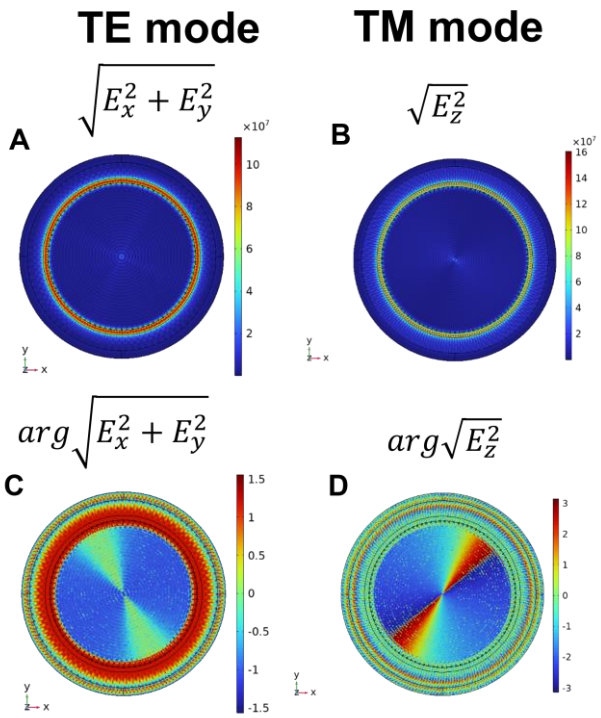

Figure S1. Simulation results on scatter field with topological charge *l*=1: (A) normalized xy-component of the electric field (TE mode), **(B)** normalized z-component of the electric field (TM mode), **(C)** phase image of the xy-component of the electric field (TE mode), **(D)** phase image of the z-component of the electric field (TM mode).

From the simulation, it is evident that TM modes are more effective at generating significant OAM through cumulative phase variations. However, separating the left-rotating and right-rotating components remains challenging. A common method for distinguishing their helical directions involves interference with right-hand circularly polarized (RHCP) or left-hand circularly polarized (LHCP) [6] beams. Meanwhile, the radial mode exhibits characteristics similar to a scalar Bessel beam [7]. The simulation shows that a zero-order Bessel beam is generated due to inner wall reflections and guided-mode resonance. For real samples, it is

anticipated that higher-order radial modes will appear as the microring size increases. Higher-order Bessel beams contain angular components, which lead to phase shifts and the transmission of orbital angular momentum. Studies have investigated separating OAM from Bessel beams based on radial direction shape asymmetry [8].

Fabrication process

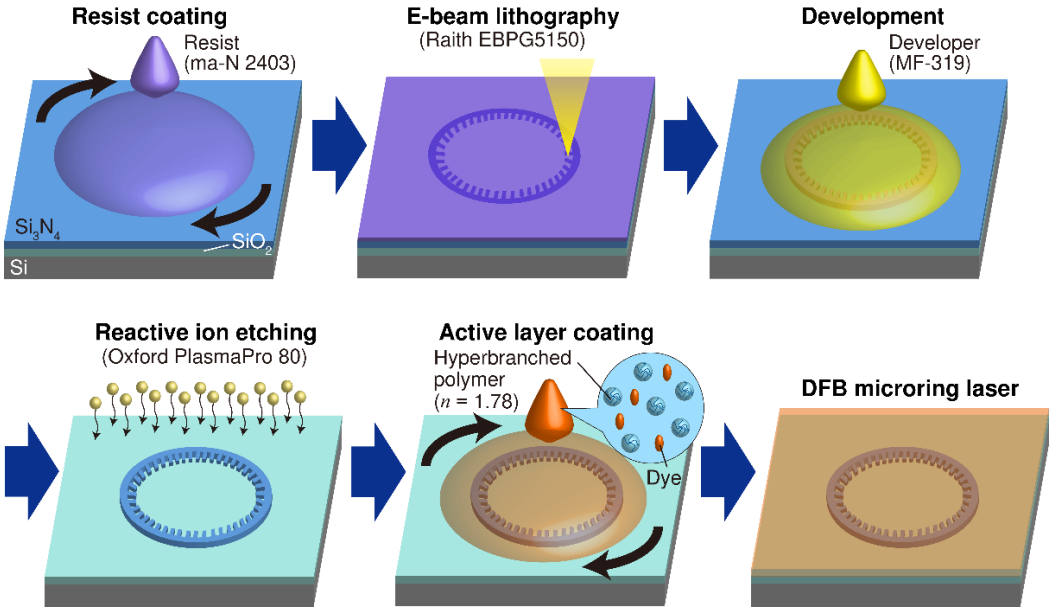

Figure S2. Procedure to manufacture active-cladding grating-integrated microring laser.

The fabrication of grating integrated Si_3N_4 microring lasers is shown in Fig. S2. The microrings were formed from Si_3N_4 deposited on SiO_2 above a Si substrate by electron-beam lithography (EBPG5150, Raith GmbH) and subsequent reactive ion etching (Oxford PlasmaPro 80). Si_3N_4 is a suitable material for lithography and etching of nanoscale structures because of its hardness and stability. The thickness of the ring was 200 nm. The active layer consisted of triazine hyperbranched polymer with n_{eff} = 1.78 (TZ-001, Nissan Chemical Co., Ltd.), doped with pyrromethene 597 (Exciton) dye with a 6.5 mM

concentration (before spin-coating). Our research lab has previously conducted research on printable dye-doped lasers [9], in which TZ-001, as a material adapted to laser dyes, has shown good performance in terms of dye degradation and stability. The active cladding thickness was set to ~200 nm by modifying the spin-coat rotation speed.

Experimental Setup

The experimental setup for excitation is shown in Fig. S3. Optical stimulation was achieved by second-harmonic generation on a Q-switched Nd: YAG laser (PNP-M08010-120, Teem Photonics) with a pulse repetition rate of 10 Hz and an operating wavelength of 532 nm. The pumping energy was nearly 0.00134 J/cm^2, varying marginally for different samples. The microring laser devices were placed on a microscope stage to facilitate excitation and light collection through confocal microscopy. A long-pass filter blocking 532 nm light ensured that the spectrometer captured only light from the microring laser.

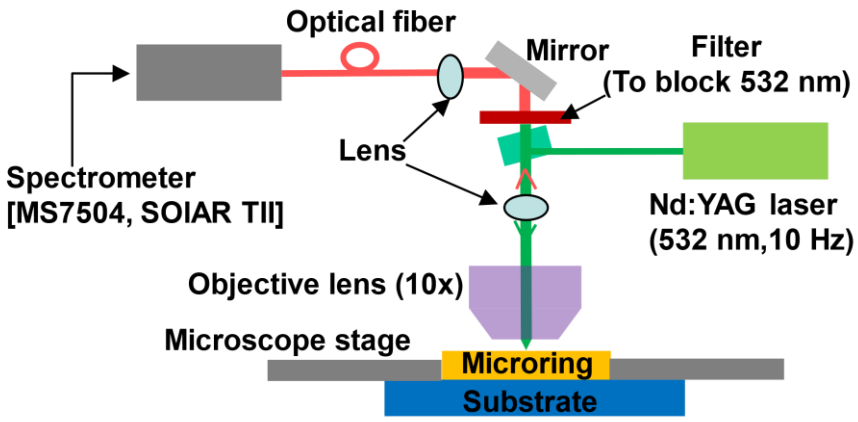

Figure S3. Schematic of the experimental setup of photoexcitation of the grating-integrated microring laser.

Reference

(1) Frateschi, N. C.; Levi, A. F. J. The Spectrum of Microdisk Lasers. *Journal of applied physics* **1996**, *80* (2), 644–653.

(2) Dubé-Demers, R.; St-Yves, J.; Bois, A.; Zhong, Q.; Caverley, M.; Wang, Y.; Chrostowski, L.; LaRochelle, S.; Plant, D. V.; Shi, W. Analytical Modeling of Silicon Microring and Microdisk Modulators With Electrical and Optical Dynamics. *Journal of Lightwave Technology* **2015**, *33* (20), 4240–4252.

(3) Ohtera, Y.; Iijima, S.; Yamada, H. Guided-Mode Resonance in Curved Grating Structures. *Optics letters* **2011**, *36* (9), 1689–1691.

(4) Ohtera, Y.; Iijima, S.; Yamada, H. Cylindrical Resonator Utilizing a Curved Resonant Grating as a Cavity Wall. *Micromachines* **2012**, *3* (1), 101–113.

(5) Lin, S. F.; Wang, C. M.; Tsai, Y. L.; Ding, T. J.; Yang, T. H.; Chen, W. Y.; Yeh, S. F.; Chang, J. Y. A Model for Fast Predicting and Optimizing the Sensitivity of Surface-Relief Guided Mode Resonance Sensors. *Sensors and Actuators B: Chemical* **2013**, *176*, 1197–1203.

(6) Cai, X.; Wang, J.; Strain, M. J.; Johnson-Morris, B.; Zhu, J.; Sorel, M.; O'Brien, J. L.; Thompson, M. G.; Yu, S. Integrated Compact Optical Vortex Beam Emitters. *Science* **2012**, *338* (6105), 363–366.

(7) McGloin, D.; Dholakia, K. Bessel Beams: Diffraction in a New Light. *Contemporary Physics* **2005**, *46* (1), 15–28.

(8) Kotlyar, V. V.; Kovalev, A. A.; Skidanov, R. V.; Soifer, V. A. Asymmetric Bessel–Gauss Beams. *JOSA A* **2014**, *31* (9), 1977–1983.

(9) Yoshioka, H.; Ota, T.; Chen, C.; Ryu, S.; Yasui, K.; Oki, Y. Extreme Ultra-Low Lasing Threshold of Full-Polymeric Fundamental Microdisk Printed with Room-Temperature Atmospheric Ink-Jet Technique. *Scientific Reports* **2015**, *5* (1), 10623.